Linear instability of a premixed slot flame: flame transfer function and resolvent analysis

Chuhan Wang, Thomas Kaiser, Max Meindl, Kilian Oberleithner, Wolfgang Polifke, Lutz Lesshafft

Linear instability of a premixed slot flame: flame transfer function and resolvent analysis

Chuhan Wang[a], Thomas Ludwig Kaiser[b], Max Meindl[c], Kilian Oberleithner[b],

Wolfgang Polifke[c], Lutz Lesshafft[a]

[a]LadHyX, CNRS, Ecole Polytechnique, Institut Polytechnique de Paris, 91120 Palaiseau, France
[b]Laboratory for Flow Instabilities and Dynamics, Technische Universität Berlin, 10623 Berlin, Germany
[c]Technische Universität München, 80333 München, Germany

Abstract

The response to forcing of a 2D laminar premixed slot flame is investigated by means of linear analysis, based on the compressible flow equations with a two-step reaction scheme for methane combustion. The flame transfer function (FTF) is computed from this linear model, in excellent agreement with reference nonlinear calculations. The input-output gain between externally applied forcing and the global heat release rate response is computed, and peaks in the gain are related to intrinsic thermoacoustic (ITA) modes. The receptivity of the flame to arbitrary flow forcing is characterised by the resulting amplitude of global heat release rate fluctuations. Linear resolvent analysis is used to identify optimal forcing structures and their associated flame response, leading to a discussion of the dominant mechanisms for the amplification of flow perturbations, which trigger flame oscillations. These seem to involve a resonance with ITA instability modes.

Keywords: combustion instability; linear instability; premixed laminar flame; flame transfer function; resolvent analysis; intrinsic thermoacoustic mode

1 Introduction

Flames are known to show unstable behaviour across nearly all technically relevant parameter regimes and configurations. Such unstable flame dynamics pose a major problem in the design of combustion systems, because they limit performance, reduce lifetime, and restrict operating conditions. In the most traditional sense, instability denotes the potential of a flame, or any flow, to develop self-sustained large-amplitude oscillations, which usually can be characterised by a temporally growing eigenmode of the linearised system of governing equations. In a larger sense, instability analysis is not limited to the description of growing eigenmodes and the ensuing "oscillator behaviour"; it can also be used to characterise the potential of a flow to *amplify* perturbations in response to external forcing ("amplifier behaviour", see [1]). These two approaches are often referred to as "modal" versus "non-modal" analysis in the literature. In the present study, we aim to characterise the non-modal amplifier behaviour of a slot flame configuration, which does not exhibit modal instability. The mechanisms that contribute to modal or non-modal instability dynamics may be intrinsic to the flame and

its supporting flow field [2], or they may involve an acoustic resonance between the flame and its surrounding chamber [3]. Chamber resonance effects, which underpin the classical thermoacoustic instability, are not investigated in this paper.

Flame instability has been approached in weakly and fully nonlinear frameworks [4, 5], but linear analysis still plays an important role in fundamental studies and industrial applications, such as sensitivity analysis, optimisation and control [6]. The linear flame transfer function (FTF), which relates fluctuations of the global heat release rate to local fluctuations of the velocity in a chosen measurement point, is widely used for the modelling of the flame response to acoustic forcing. Classically, the flame transfer function is obtained from experiments or numerical simulations via empirical system identification methods based on time-series of forcing and response data. This strategy is data-driven, and represents a *black-box* approach [7]. We advocate here an alternative strategy, based on the linear flow equations, which may be described as a *white-box* method. To this end, we linearize the governing equations and calculate the Jacobian matrix around a steady base flow state, which is obtained as a fixed point of the nonlinear system of equations. The resulting linear system governs the dynamics of small-amplitude fluctuations, and it can be accessed with a large variety of linear tools for a physics-based analysis. Note that our objective is not to create analytical models of the FTF, as one might do for instance by using a G-equation [8]. The single hypothesis that we employ here is that we work with fluctuations of small amplitudes in the linear limit. The complete set of linearized governing equations and the information of each flow variable in the base flow is preserved.

This method allows efficient calculation of the FTF, because no time-stepping is required. A pioneering attempt in this direction was made by van Kampen *et al.* [9] to reduce the computational burden of FTF calculations by use of a "linear coefficient method", based on the response of flow variables to small-amplitude perturbations. The response of global heat release rate to the fluctuation of inlet equivalence ratio was investigated for a turbulent swirling flame. The response obtained via the linear coefficient method was reported to be in good agreement with reference calculation results. Nevertheless, this method does not include some essential characteristics of the flame dynamics, such as the effect of equivalence ratio fluctuations on the flame front movement. The approach used in the present study fully encompasses those effects.

Another important feature is that the white-box method gives spontaneously a *multi-input, multi-output* (MIMO) system. While the classical flame transfer function is represented as a *single-input, single-output* (SISO) system associating the heat release rate with velocity disturbances, one may also want to explore other physical quantities in flames. A MIMO formulation is required if one wants to, for instance, compute the flame responses to incoming fluctuations of the mixture composition [10, 11, 12, 13, 14], or represent acoustic scattering [15, 16]. MIMO systems can in principle be identified with black-box methods, but special technical considerations are necessary, for instance so as to ensure statistical independence among different signal channels [7, 17]. A linear approach, as presented in this study, inherently preserves the causal coupling between all signals, and all mappings can be extracted from one linear system.

The applicability of linear analysis to flame dynamics has already been demonstrated in several recent studies, for premixed as well as diffusion flames. Throughout this paper, the linear analysis is carried out in a *global* setting, i.e. on a spatially developing base flow, in contrast to *local* analysis which is based on the assumption of a streamwise-invariant base flow. For reacting flows, local analysis has indeed been successfully applied in reacting bluff-body wakes that can be regarded as being weakly non-parallel [18]. This assumption however does not hold for most flames, so we use global analysis where the word "global" means that the variations in the base flow are resolved both in the streamwise and in the cross-stream direction. A brief state-of-the-art survey is given for such studies on premixed flames. The reader may want to refer to [19, 20, 21, 22, 23] for work on diffusion flames.

Investigating the role of precessing vortex core (PVC) dynamics in combustion instability, Oberleithner *et al.* [24, 25] performed modal analysis on experimental data of turbulent flames in a swirl combustor. A solver based on the linearized incompressible Navier-Stokes equations with an eddy-viscosity model was applied. The predicted frequency of the instability mode was found to be in excellent agreement with the oscillation frequency measured in the experiment. For other linear calculations with regard to the PVC, the reader may refer to [26, 27].

Blanchard *et al.* [28] developed a linear solver based on the compressible Navier-Stokes equations with a one-step

chemistry scheme. The FTF of a steady M-shaped premixed laminar flame was calculated. The frequencies with maximum and minimum FTF gain were correctly retrieved, with respect to experimental measurements, but discrepancies in the gain values remained, presumably due to the simplicity of the chemistry model. By performing non-modal analysis, the authors characterized the physical interactions that give rise to pressure wave generation in the flame front [29]. This study was recently extended to swirling M-flames by Skene *et al.* [30].

Recent work on premixed laminar flames, by Polifke and coworkers [31, 32, 33], is highly relevant to the present study. The objective of Avdonin *et al.* [31] was to introduce a new approach that can accurately predict FTFs and thermoacoustic modes. The linearized reactive flow approach (LRF) that contains the set of equations of a reacting flow, was used to calculate the FTF, quantitatively validated against results obtained by nonlinear timestepping. The global eigenmodes were then calculated with the LRF solver. Due to the limitation of the computational domain, the thermoacoustic mode associated with the combustion chamber could not be captured. Instead, another scenario of acoustic feedback taking place within the flame was identified. Such a scenario independent of the chamber mode is known as the intrinsic thermoacoustic instability (ITA) mode [34, 35, 36]. Global eigenmodes were found at the frequencies where the ITA modes are expected to occur. The unstable eigenmode structures showed a distortion of the flame front induced at the flame root. Entropy waves generated by acoustically forced premixed slot flames, including a freely propagating 1D flame and a 2D slot flame, were calculated [33], via the LRF approach and a hybrid approach that combined the linearized incompressible Navier-Stokes equations and the FTF (LNSE+FTF approach). The LNSE+FTF approach generated spurious entropy waves, whereas the entropy waves as well as the FTF obtained through the LRF are in quantitative agreement with reference results. The LRF solver was also used to study the interaction between inertial waves and flames [32]. The inertial waves have non-zero axial and radial components, which bring the flame out of kinematic balance and thereby cause changes in flame shape and heat release. The flame front was found to be modulated mainly by axial and radial velocity fluctuations associated with inertial waves.

In closely related fields, global linear analysis has been widely applied with great success in shear flows where instability dynamics lead to an amplification of external perturbations [37]. Such dynamics are commonly investigated by means of *resolvent analysis*; this formalism can be applied to laminar as well as turbulent flow regimes, as demonstrated for jets [38, 39, 40], backward-facing step flow [41] and channel flow [42, 43], among other configurations. In the resolvent framework, optimal forcing and associated flow response structures are identified in the frequency domain to quantitatively analyse the amplification of flow perturbations. In recent years, resolvent analysis has been applied also to the configuration of turbulent flames. Kaiser et al. [44] showed that the method is able to model the hydrodynamic response of a swirled flame to acoustic perturbations. Casel et al. [45] further demonstrated the capabilities of the resolvent analysis to model the dominant coherent hydrodynamic structures in a fully turbulent Bunsen flame. Note however, that these two studies do not account for coherent fluctuations of heat release rate, which restricts these analyses to purely hydrodynamic mechanisms.

In the present work, we construct a linear reacting flow model, on which we base a discussion of the physical mechanisms that lead to selective amplification of certain frequencies in the flame. Linear analysis of multi-physics dynamics in a laminar slot flame obtained from nonlinear simulation is presented, where two spatial dimensions are resolved. In the framework of resolvent analysis, we identify the precise flow forcing that elicits maximally energetic flame oscillations. Specifically, one of the configurations that we are interested in is the flame response to perturbations of fuel equivalence ratio. The resolvent analysis can shed light on the most "dangerous" structures that lead to the maximal flame response, which can inform a detailed discussion of the physical mechanisms of perturbation amplification. Our linear model accounts for the non-parallelism of the flow field, for chemical reaction, and for the coupling of acoustic and vortical perturbations. Reactions are modelled by a two-step chemical scheme.

The paper is organized as follows. In Section 2, the steady flame configuration is presented, which is used as a base flow in the following linear analysis. In Section 3, the nonlinear governing equations are documented, including details of the chemical scheme, and the linearized system is introduced. The FTF is calculated in Section 4 with boundary forcing, which serves as a validation of our linear system with respect to that obtained from nonlinear timestepping. To quantify the efficiency of the flame actuation in the FTF scenario, an input-output analysis is then introduced. In Section 5, the

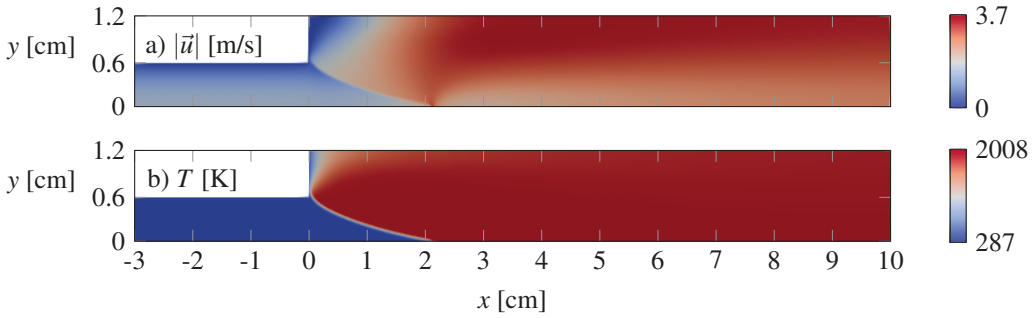

Figure 1: Steady base flow state, obtained from nonlinear simulation with AVBP: a) velocity magnitude; b) temperature. The numerical domain resolves half of the flame, with a symmetry condition at the center line ($y = 0$).

influence of arbitrary forcing on the global heat release rate is characterized via a receptivity analysis. Finally, resolvent analysis is conducted in Section 6 with optimisation norms of different physical quantities. Conclusions and perspectives are given in Section 7.

2 Nonlinear simulation of a steady slot flame

We perform a time-discrete, fully nonlinear laminar direct numerical simulation of a two-dimensional perfectly premixed slot flame.

The time stepping is performed using the AVBP code developed by CERFACS [46], which solves the governing equations using the cell-vertex method. The two step Taylor-Galerkin method (TTGC) [47] is applied for the discretization of the advective term, which, for the triangular grid, is third-order accurate in space and time. For the diffusive fluxes an adaptation of the finite-element Galerkin method to the cell-vertex method is applied [48]. The reaction chemistry is modelled by the BFER scheme [49]. The model accounts for six transported species and two reactions. The reactions are based on an Arrhenius term with pre-exponential correction factors, which assure correct laminar flame speeds over a large range of fresh gas temperatures, pressures and equivalence ratios.

The flow domain is 10 cm long and 2.4 cm wide, including an inflow channel of length 3 cm and width $H = 1.2$ cm. A symmetry condition along the centerline $y = 0$ allows us to restrict the calculations to the half-domain, shown in figure 1. The inflow conditions for bulk speed, temperature and equivalence ratio are chosen as

$$U = 1\frac{\mathrm{m}}{\mathrm{s}},\ T_0 = 287\mathrm{K},\ \phi = 0.8. \tag{1}$$

This results in an inflow Reynolds number $\mathrm{Re} = \rho_0 U H/\mu_0 = 728$, where ρ_0 and μ_0 denote the density and the dynamic viscosity at the inflow, respectively.

At the inlet and at the outlet, Navier-Stokes characteristic boundary conditions (NSCBC) are applied [50]. An acoustically hard inlet condition is used at the inlet, where a parabolic velocity profile is prescribed. An acoustically soft outlet condition lets acoustic waves exit the domain with minimal reflection. The no-slip wall boundaries at ($x < 0$, $y = 0.6$ cm) and ($x = 0$, $y > 0.6$ cm) are isothermal, where the temperature is equal to the one of the unburnt gas, T_0. In addition to the symmetry boundary condition at the center plane of the flame, a second symmetry condition is applied at the upper boundary ($y = 1.2$ cm).

3 Methods

3.1 Nonlinear governing equations

The compressible reactive flow equations, which are to be linearized around the base state for the following analysis, are formulated in terms of conservative variables (ρ, ρu, ρv, ρh, ρY_k) in Cartesian coordinates (x, y), where (u, v) are the streamwise and cross-stream velocity components, ρ is the density, h is the sensible enthalpy and Y_k is the mass fraction of species k. Following the notation of Avdonin *et al.* [31], these equations are given as

$$\frac{\partial \rho}{\partial t} = -\frac{\partial}{\partial x_j}(\rho u_j), \tag{2}$$

$$\frac{\partial \rho u_i}{\partial t} = -\frac{\partial}{\partial x_j}\left(\rho u_i u_j\right) - \frac{\partial p}{\partial x_i} + \frac{\partial \tau_{ij}}{\partial x_j}, \tag{3}$$

$$\frac{\partial \rho Y_k}{\partial t} = -\frac{\partial}{\partial x_j}\left(\rho u_j Y_k\right) - \frac{\partial J_j}{\partial x_j} + \dot{\omega}_k, \tag{4}$$

$$\frac{\partial}{\partial t}(\rho h - p) = -\frac{\partial}{\partial x_j}(\rho u_j h) - \frac{\partial q_j}{\partial x_j} + \dot{\omega}_T, \tag{5}$$

closed with the equation of state for an ideal gas $p = R_s \rho T$, where p is the pressure, T is the temperature, and R_s is the specific gas constant. The molecular stress tensor is given by $\tau_{ij} = -\frac{2\mu}{3}\frac{\partial u_k}{\partial x_k}\delta_{ij} + \mu\left(\frac{\partial u_i}{\partial x_j} + \frac{\partial u_j}{\partial x_i}\right)$. The molecular viscosity μ is modelled by a power law $\mu = c_1(T/T_{\text{ref}})^b$, with tabulated constants c_1, T_{ref} and b. The flux of species transport and heat transfer are modelled as $J_j = -D_k\frac{\partial Y_k}{\partial x_j}$ and $q_j = -\alpha\frac{\partial h}{\partial x_j}$, respectively. The transport coefficients are related by a Schmidt number $\text{Sc}_k = \frac{\mu}{D_k}$ for species k and a Prandtl number $\text{Pr} = \frac{\mu}{\alpha}$. Constant values $\text{Sc}_k = 0.7$ and $\text{Pr} = 0.7$ are chosen for the lean methane-air mixture, as prescribed in the BFER chemical scheme. For a mixture of N species, the aggregate sensible enthalpy is defined as $h = \sum_{k=1}^{N} h_k Y_k$, where the sensible enthalpy of species k is defined as $h_k = \int_{T_0}^{T} C_{p,k} dT$. The sensible enthalpy h_k and the heat capacity $C_{p,k}$ are linearly interpolated from JANAF tables through the same method as in AVBP.

The reaction rate $\dot{\omega}_k$ of species k, and the heat release rate due to combustion $\dot{\omega}_T$, are modelled by the two-step BFER chemistry scheme, based on the Arrhenius law. The reaction rate $\dot{\omega}_k$ for a chemistry scheme of overall M reactions is defined by $\dot{\omega}_k = W_k \sum_{j=1}^{M} \nu_{kj} Q_j$, where W_k is the molecular mass of species k, ν_{kj} is the molar stoichiometric coefficient of species k in reaction j, and Q_j is the progress rate of reaction j. The heat release rate is defined by $\dot{\omega}_T = -\sum_{j=1}^{M} \Delta h^o_{f,j} Q_j$, where $\Delta h^o_{f,j}$ denotes the standard enthalpy of reaction corresponding to reaction j.

The BFER chemical scheme involves six species (CH_4, O_2, CO_2, CO, H_2O, N_2) and two reactions,

$$CH_4 + 1.5O_2 \rightarrow CO + 2H_2O, \tag{6}$$

$$CO + 0.5O_2 \rightleftharpoons CO_2. \tag{7}$$

The second reaction describing the equilibrium between CO and CO_2 is reversible. The progress rates Q_1 and Q_2 are given by

$$Q_1 = \kappa_{f,1}[X_{CH_4}]^{n_{1,CH_4}}[X_{O_2}]^{n_{1,O_2}}, \tag{8}$$

$$Q_2 = \kappa_{f,2}[X_{CO}]^{n_{2,CO}}[X_{O_2}]^{n_{2,O_2}} - \kappa_{r,2}[X_{CO_2}]^{n_{2,CO_2}}, \tag{9}$$

where $[X_k]$ is the molar concentration of species k defined by $[X_k] = \rho \frac{Y_k}{W_k}$. The forward reaction rate constant for reaction j is modelled by the Arrhenius law

$$\kappa_{f,j} = A_j f_j(\phi) T^{\beta_j} \exp\left(-\frac{T_{a,j}}{T}\right), \tag{10}$$

where f_j is a correction function with respect to equivalence ratio ϕ. The backward rate constant is linked to the forward rate via an equilibrium constant K as

$$\kappa_{r,2} = \frac{\kappa_{f,2}}{K}. \tag{11}$$

Values for the model constants A_j, $T_{a,j}$, β_j and n_j are taken from the BFER tables [49]. In the study of Meindl et al. [33], a different two-step chemical scheme (2S_CH4_CM2) was used, and the coefficients in the reaction model are not the same. In both studies, the equivalence ratio is 0.8, so both reaction models should be suitable to produce the correct flame properties [51].

3.2 Linear analysis

The dynamics of small-amplitude fluctuations around a steady flow state are governed by linear equations. In what follows, we decompose the state variables $\boldsymbol{q} = (u, v, \rho, p, Y_k)$ into a base flow component $\bar{\boldsymbol{q}}$ and a fluctuation component $\boldsymbol{q'}$. This decomposition is introduced into Eqs. (2)-(5), and the terms are arranged into the form

$$\frac{\partial \boldsymbol{B q'}}{\partial t} - \boldsymbol{A q'} = \boldsymbol{P f'}, \tag{12}$$

following the linearized governing equations (26-29) given in the Appendix. All terms linear in $\boldsymbol{q'}$ are on the left-hand side in Eq. (12), whereas all terms nonlinear in $\boldsymbol{q'}$ are replaced by the vector $\boldsymbol{f'}$, which is interpreted as a forcing input into the linear system [42, 39]. More specifically, for the following analysis, the vector $\boldsymbol{f'}$ contains all non-zero forcing components, and the matrix $\boldsymbol{P}$ adds zero elements as required for the dimension of the linear system. $\boldsymbol{P}$ is therefore a rectangular matrix with only 0 and 1 as elements. The forcing vector $\boldsymbol{f'}$, in addition to the intrinsic forcing by nonlinear terms, may also represent external forcing that is applied at the domain boundaries. In this work, we consider forcing on streamwise velocity f_u, transverse velocity f_v, and fuel concentration $f_{\mathrm{CH_4}}$. In the following, we will consider time-harmonic forcing $\boldsymbol{f'} = \hat{\boldsymbol{f}} e^{\mathrm{i}\omega t}$ at frequency $\frac{\omega}{2\pi}$, and its associated time-harmonic response $\boldsymbol{q'} = \hat{\boldsymbol{q}} e^{\mathrm{i}\omega t}$. This leads to a relation between $\hat{\boldsymbol{q}}$ and $\hat{\boldsymbol{f}}$ in the frequency domain

$$(\mathrm{i}\omega \boldsymbol{B} - \boldsymbol{A})\, \hat{\boldsymbol{q}} = \boldsymbol{P} \hat{\boldsymbol{f}}. \tag{13}$$

In what follows, we use the flame Strouhal number $St = \frac{\omega H}{4\pi S_L}$ as a non-dimensional frequency [28], where the laminar burning velocity S_L is 0.29 m/s and the slot half-width $H/2$ is 0.6 cm.

The cumbersome linearization of the governing equations (2)-(5) is performed, as far as possible, by use of the symbolic calculus functionality provided by the Unified Form Language (UFL, see [52]). However, a few terms, like for example the sensible enthalpy interpolated from JANAF tables, require linearization by hand. We reduce the number of linearized species equations from six to four by transporting only CH_4, O_2, CO_2 and CO, and regarding H_2O and N_2 as passive scalars. More details about the linearization process are documented in the Appendix. It is important to keep in mind that Eqs. (2-5), from which our linear system is derived, are not strictly identical to those solved in the AVBP code, although we strived to stay close to this reference.

At the inlet and the outlet of the numerical domain, stress-free boundary conditions are imposed. These are a standard choice in finite element formulations for open boundaries (see for instance [38]), generally found to have a weak influence on the dynamics in the domain interior. It has been checked that the numerical domain length has a negligible effect on the results of FTF, therefore the upstream and downstream boundary conditions can be considered to be appropriately

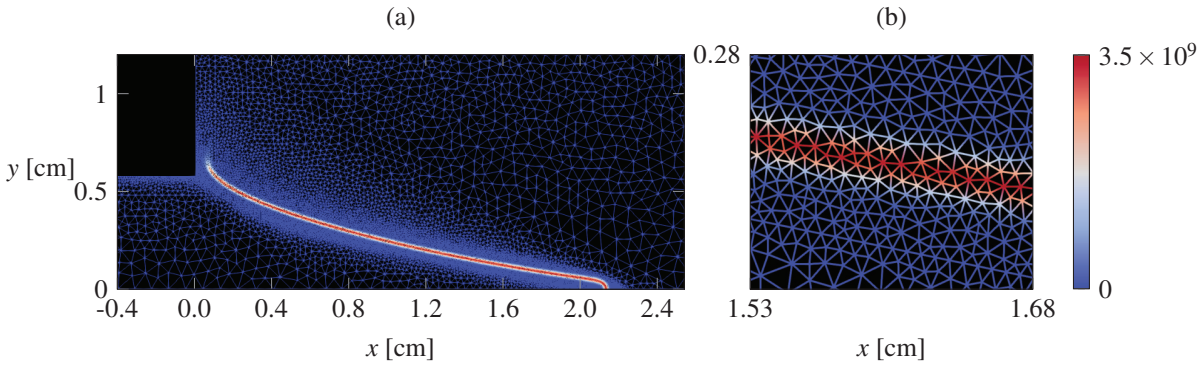

Figure 2: A portion of the standard mesh that is used throughout this study. Colors represent the base flow heat release rate $\dot{\omega}_T$ [J/m^3/s] in order to visualize the flame front position.

transparent. At the inlet, the fluctuations of density and mass fraction of each species are set to zero. The fluctuations of velocity and density are set to zero along the wall. Cross-stream velocity fluctuations are set to zero at the centerline and at the upper boundary, consistent with the symmetry conditions used in AVBP.

The linear system and all analysis tools are implemented in Python, making strong use of the FEniCS framework. The continuous Galerkin method is used to discretize the partial differential equations on unstructured meshes, with finite elements of quadratic order.

The mesh used in the AVBP computations contains 450,358 cells, which is not easily affordable for matrix operations in the linear analysis. The base flow is therefore interpolated on a less refined mesh of 19,278 elements for linear calculations, shown in Fig. 2. High spatial resolution is maintained in the reaction region and near walls.

4 The flame transfer function

4.1 Validation of the linear solver versus AVBP

For validation purposes, the flame transfer function (FTF) is computed with our linear solver, and compared to reference results obtained with AVBP. Such a validation strategy has already been used in [28] against the experimental data, and in [31, 32, 33] quantitatively against the nonlinear timestepping results. The FTF is defined as

$$F(\omega) = \frac{\bar{u}_{\mathrm{ref}}}{\bar{\dot{\Omega}}_T} \frac{\dot{\Omega}'_T}{u'_{\mathrm{ref}}}, \tag{14}$$

relating normalized fluctuations of the global heat release rate to those of a reference velocity. These two quantities are defined as $\dot{\Omega}_T = \iint \dot{\omega}_T \mathrm{d}x\mathrm{d}y$, integrated over the entire computational domain, and u_{ref} the vertically averaged inflow velocity. As before, overbars denote base flow quantities, and primes denote fluctuations.

To obtain the reference FTF based on the AVBP simulations, the Wiener-Hopf inversion, a method of system identification, is performed. Instead of determining the FTF based on harmonic forcing frequency by frequency, the Wiener-Hopf inversion allows to apply a broad-band forcing, which also results in broad-band fluctuations in the heat release rate. The FTF is then determined in the post processing based on a statistical evaluation of the velocity fluctuations and the resulting heat release rate fluctuations. For more details on the method, the reader is kindly referred to [17, 53].

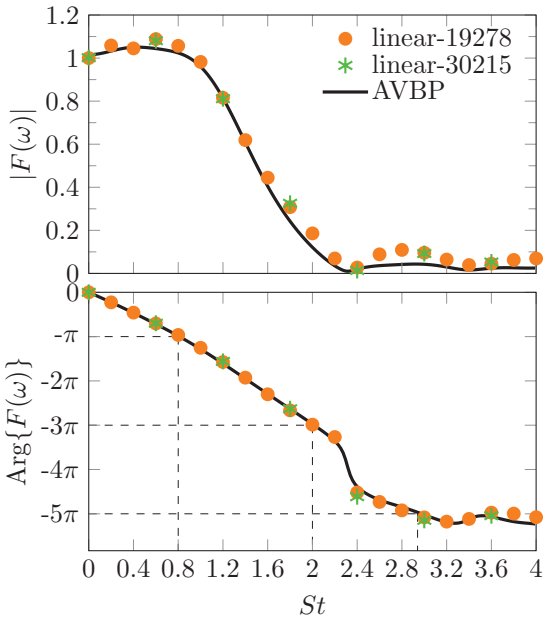

Figure 3: Flame transfer function: result obtained from AVBP by nonlinear timestepping with broad-band inflow boundary forcing, alongside results obtained from the linear solver through harmonic inflow boundary forcing with meshes of 19278 and 30215 elements. The auxiliary lines mark the phases at odd multiples of π associated with intrinsic thermoacoustic instability.

The amplitude of perturbation velocity is chosen as 1% of the mean inflow velocity, such that the flow response can be considered to be in the linear regime. Modulus and phase of the FTF are shown in Fig. 3, and the harmonic flame response structures obtained from AVBP are visualized in the upper half of Fig. 4(a-h).

Corresponding calculations with our linear solver involve the solution of a matrix-vector problem, given by Eq. (13), for a given frequency. Consistent with the nonlinear simulation, the volume forcing $\hat{\boldsymbol{f}}$ is set to zero in these calculations, and the system is forced instead by a non-homogeneous Dirichlet boundary condition on the streamwise velocity fluctuations $\hat{\boldsymbol{u}}$ at the inflow. A typical calculation for one frequency value requires about 6 minutes on a single core (Intel i7-8700K, 3.70GHz), which is significantly cheaper than a corresponding AVBP run. Note that in AVBP for such a single harmonic calculation, the nonlinear timestepping over one period requires between 500 and 1000 CPU hours, depending on the frequency.

The FTFs obtained with both methods are compared in Fig. 3, and it is found that the linear solver accurately reproduces the AVBP results. Convergence of the linear calculations with respect to spatial resolution is confirmed by comparing the results from two different meshes. The coarser mesh, composed of 19278 triangular elements as shown in Fig. 2, will be used throughout this study. For further validation, snapshots of the linear flow response to harmonic inflow forcing at $St = 0.8$ are compared in Fig. 4 to the nonlinear simulation results, for several fluctuation quantities, and excellent agreement is observed.

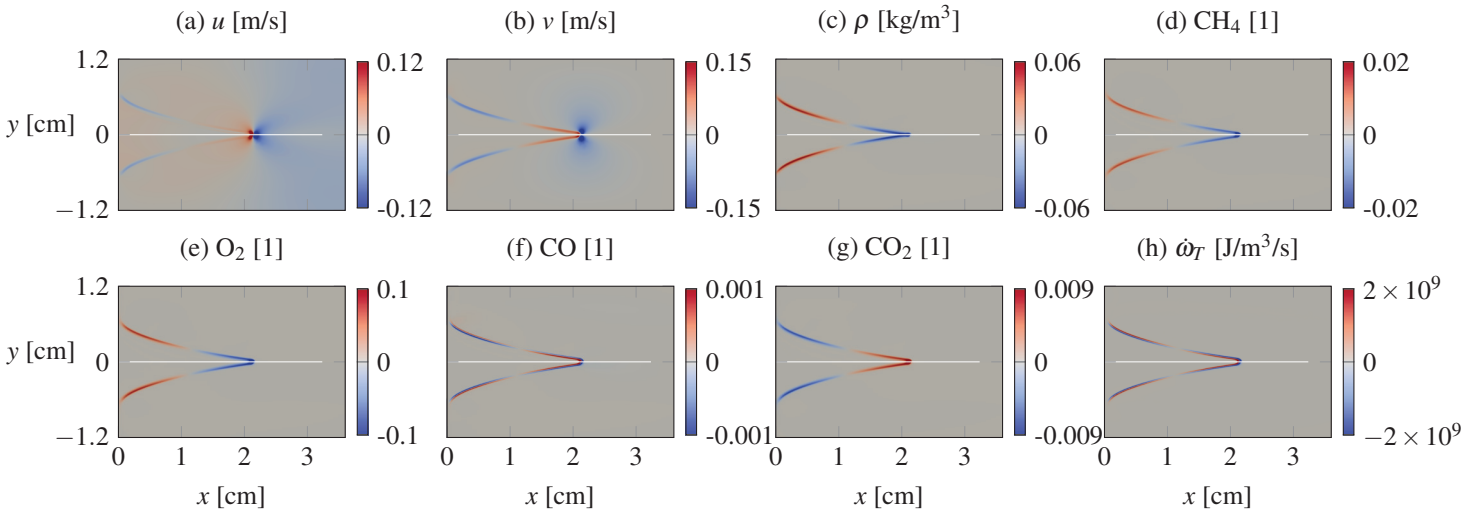

Figure 4: Response to inflow velocity forcing at $St = 0.8$. Upper half: nonlinear (AVBP); lower half: linear.

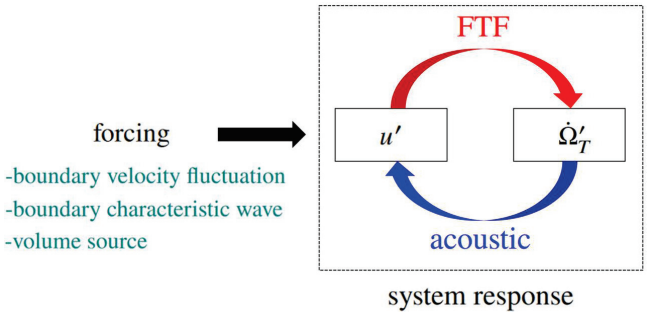

Figure 5: Illustration of the input/forcing and output/response. The FTF is established inside the response field.

4.2 Input-output gain

There are generally three ways to force fluctuations in a flame in numerical simulations. The first method is to prescribe an inflow velocity fluctuation, as has been done in the previous section. The second method is to specify an incoming acoustic wave through a characteristic boundary condition [54, 55]. The third method is to introduce a source term in the governing equations, as is done in [28]. Any of these methods will induce a response of the flame. The FTF relates the global heat release rate fluctuation to an upstream velocity fluctuation, both of which are part of the flow response to the externally applied forcing. The FTF does not, however, relate the system response to the forcing input, as shown in Fig. 5.

We are interested in the question, how strongly the flame reacts to external forcing input of a given type and frequency. To this end, the forcing (input) and the response (output) must be measured by appropriate norms. For instance, previous flame studies [54, 55] identified the ratio of incoming (input) and outgoing (output) acoustic wave amplitudes at the inflow boundary. It was found that the peaks of this amplitude gain do not coincide with those of the FTF gain.

We consider an external input in the form of volume forces f_u and f_v, as defined in Section 3.2, measured by their

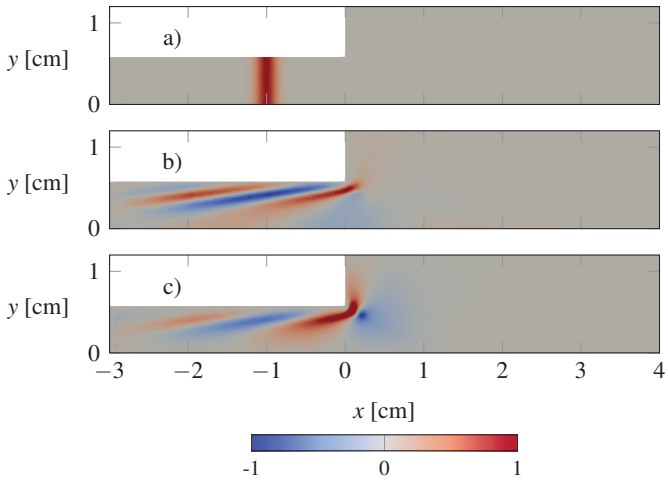

Figure 6: (a) flat Gaussian forcing $\hat{f}_G$ with $x_c = -1$ cm and $w = 0.2$ cm on $\hat{f}_u$. b) receptivity field $\hat{\boldsymbol{r}}$ on $\hat{r}_u$. c) receptivity field $\hat{\boldsymbol{r}}$ on $\hat{r}_v$. The receptivity is calculated at $St = 0.8$. All the fields are normalised with their maximum value.

standard 2-norm,

$$\|\hat{\boldsymbol{f}}\|^2 = \iint_\Omega \left(|\hat{f}_u|^2 + |\hat{f}_v|^2\right) \mathrm{d}x\mathrm{d}y. \tag{15}$$

The flame response, as an output, is measured by the global heat release rate fluctuation $\hat{\Omega}_T$, consistent with the FTF definition. The *input-output gain* is then defined as

$$\sigma^2 = \frac{\hat{\Omega}_T^2}{\|\hat{\boldsymbol{f}}\|^2}. \tag{16}$$

We first design a volume force term that should allow us to reproduce the FTF. A Gaussian distribution in x, independent of y, is prescribed for the streamwise force component,

$$\hat{f}_G(x, y) = \exp\left[-\frac{(x - x_c)^2}{w^2}\right], \tag{17}$$

as is shown in Fig. 6(a). The flame response is obtained as the solution of the linear system in Eq. (13), for two different center positions x_c and distribution widths w. A homogeneous Neumann condition on u at the inflow permits a non-zero volume flux across the boundary in the flow response. The FTF is evaluated according to the definition of Eq. (14) (u_{ref} still is the vertically averaged inflow velocity). The results are in excellent agreement with the FTF obtained by boundary forcing at inlet, as shown in Fig. 7. This demonstrates the equivalence between the designed volume forcing and the boundary forcing. The parameters x_c and w of the Gauss distribution have no influence on the FTF results.

The input-output gain σ^2 achieved by this forcing is shown, as a function of Strouhal number, as a blue line in Fig. 8. The gain is highest at low Strouhal numbers, with a peak at $St = 0.8$. At the lowest value in our computations, $St = 3\times10^{-5}$, the gain is $\sigma^2 = 1.2\times10^4$; note that, contrary to the FTF, the definition in Eq. 16 does not lead to an expected input-output gain value of unity at zero Strouhal number.

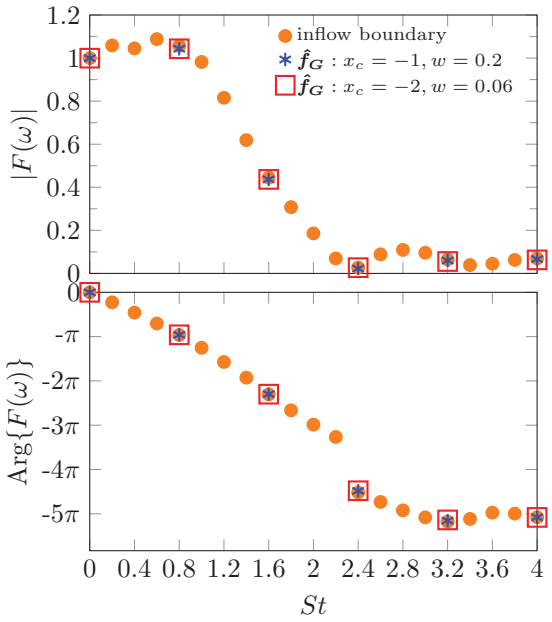

Figure 7: FTF obtained through inflow boundary forcing (same as linear-19278 in Fig. 3) and through volume forcing $\hat{f}_G$ with ($x_c = -1$, $w = 0.2$) and ($x_c = -2$, $w = 0.06$). The units of x_c and w are centimeters.

5 Receptivity of global heat release rate fluctuations to arbitrary forcing

The input-output gain, as defined in Section 4.2 for a prescribed volume forcing, can be conveniently evaluated for arbitrary spatial distributions $\hat{\boldsymbol{f}}$ through the introduction of the flame *receptivity*, as will be shown in this section.

We first define the *resolvent* operator $\boldsymbol{R}(\omega)$ by inverting the linear system of Eq. (13),

$$\hat{\boldsymbol{q}} = \boldsymbol{R}(\omega)\boldsymbol{P}\hat{\boldsymbol{f}}, \quad \boldsymbol{R}(\omega) = (\mathrm{i}\omega\boldsymbol{B} - \boldsymbol{A})^{-1}. \tag{18}$$

Note that this inversion is well defined, except in the singular case when ω is an eigenvalue of the system.

The integrated global heat release rate fluctuation, associated with the flame response $\hat{\boldsymbol{q}}$, is then given by

$$\hat{\bar{\Omega}}_T = \iint \hat{\omega}_T \mathrm{d}x\mathrm{d}y = \boldsymbol{m}_{\boldsymbol{\Omega}}{}^{\mathsf{H}}\hat{\boldsymbol{q}}, \tag{19}$$

where the vector $\boldsymbol{m}_{\boldsymbol{\Omega}}$ is constructed from the mesh quadrature coefficients of the volume integral, and from the linearization of local heat release rate according to Eq. (34) in the Appendix together with all the linearized progress rates in Eqs. (30-32). The superscript H denotes the transpose conjugate. With Eqs. (18) and (19), we find that the global heat release rate fluctuation (a complex scalar) in response to an arbitrary forcing $\hat{\boldsymbol{f}}$ (a complex vector) is obtained from a scalar product,

$$\hat{\bar{\Omega}}_T = \boldsymbol{m}_{\boldsymbol{\Omega}}{}^{\mathsf{H}}\boldsymbol{R}\boldsymbol{P}\hat{\boldsymbol{f}} = \boldsymbol{r}^{\mathsf{H}}\boldsymbol{M}\hat{\boldsymbol{f}}. \tag{20}$$

We define $\boldsymbol{r} = \boldsymbol{M}^{-1}\boldsymbol{P}^{\mathsf{H}}\boldsymbol{R}^{\mathsf{H}}\boldsymbol{m}_{\boldsymbol{\Omega}}$ as the *receptivity* vector. Note that the receptivity vector depends on the prescribed Strouhal number, as inherited from the resolvent operator, but this dependence is not written in the following for ease of

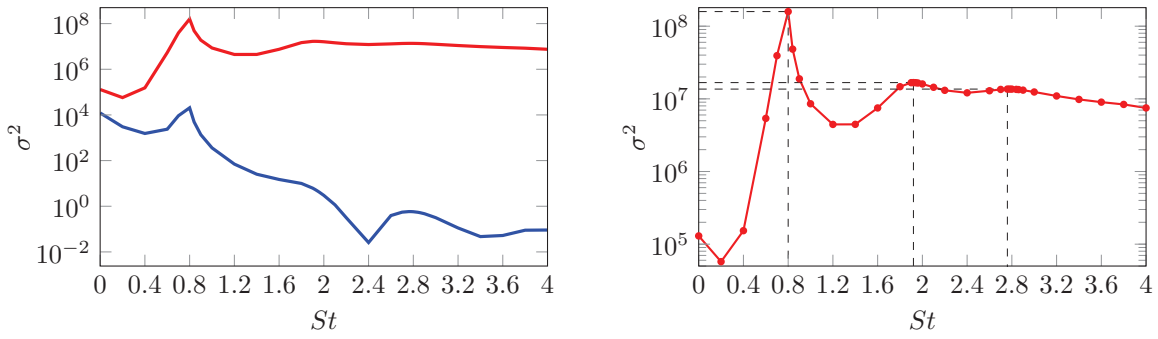

Figure 8: Input-output gain σ^2 over frequency, for Gaussian forcing $\hat{f}_G$ (blue line) and for optimal forcing $\hat{f}_{\text{opt}}$ (red line). Only $\hat{f}_{\text{opt}}$ is shown on the right. The auxiliary lines mark the local maximums of σ^2.

notation. The symmetric matrix $\boldsymbol{M}$ represents the mesh quadrature for a scalar product $\langle \boldsymbol{a}, \boldsymbol{b} \rangle_{\boldsymbol{M}} = \boldsymbol{a}^{\mathsf{H}} \boldsymbol{M} \boldsymbol{b}$, where $\boldsymbol{a}$ and $\boldsymbol{b}$ are complex-valued vectors.

As the global heat release rate amplitude $\hat{\Omega}_T$, in response to any forcing input $\hat{\boldsymbol{f}}$, is given by the projection of $\hat{\boldsymbol{f}}$ onto the receptivity $\boldsymbol{r}$, any forcing component $\hat{\boldsymbol{f}}_\perp$ that is perpendicular to $\boldsymbol{r}$, $\boldsymbol{r}^{\mathsf{H}} \boldsymbol{M} \hat{\boldsymbol{f}}_\perp = 0$, does not lead to fluctuations of the global heat release rate. Therefore, the maximum input-output gain in the sense of Eq. (15) is achieved by forcing that is proportional to $\boldsymbol{r}$, $\hat{\boldsymbol{f}}_{\text{opt}} = \alpha \boldsymbol{r}$ with $\alpha \in \mathbb{C}$. The gain for this optimal forcing is found to be

$$\sigma^2_{\text{max}} = \frac{(\boldsymbol{r}^{\mathsf{H}} \boldsymbol{M} \alpha \boldsymbol{r})^2}{(\alpha \boldsymbol{r})^{\mathsf{H}} \boldsymbol{M} \alpha \boldsymbol{r}} = \boldsymbol{r}^{\mathsf{H}} \boldsymbol{M} \boldsymbol{r}, \tag{21}$$

the squared norm of the receptivity vector.

In the following application of this receptivity formalism, for a consistent comparison with the FTF calculations in Section 4, we consider a forcing of the momentum equations, $\hat{\boldsymbol{f}} = (\hat{f}_u, \hat{f}_v)^{\mathsf{T}}$. For numerical reasons, we allow forcing only in the domain interior, imposing $\hat{\boldsymbol{f}} = 0$ on all boundaries. The resulting receptivity fields $\boldsymbol{r}$ (real parts of the x- and y-components) are presented in Fig. 6(b,c). It is found that the global heat release rate is receptive to wavy perturbations in the inflow duct, and that the receptivity is particularly high near the flame foot.

The *optimal* input-output gain $\|\boldsymbol{r}\|^2$ is plotted over frequency in Fig. 8 (red line), alongside the gain curve obtained for the non-optimal forcing used in the FTF computations (blue line). A resonance peak can be identified at $St = 0.8$ in the optimal gain.

We hypothesise that this resonance peak is related to an acoustic feedback mechanism, of the intrinsic thermoacoustic (ITA) type: according to [34, 56], ITA modes may arise when the FTF phase is equal to an odd multiple of π. The frequencies at which this criterion is fulfilled are identified as $St = 0.8$, $St = 2.0$ and $St = 2.94$ from Fig. 3. The optimal gain peak at $St = 0.8$ in Fig. 8 is therefore fully consistent with the π-criterion. It appears that this peak marks a resonance of the forcing with slightly stable ITA modes of the flame. Two local maxima with smaller amplitudes can also be identified in the optimal gain curve at $St = 1.92$ and $St = 2.76$, which are close to the other two predicted ITA Strouhal numbers.

6 Resolvent analysis

In Section 4, we used the input-output form of the linear system to define a gain between the norm of a prescribed forcing and the amplitude of the integrated heat release rate in the associated flame response. The result was a relation between

an input scalar (the forcing amplitude) and an output scalar (the global heat release rate amplitude). In Section 5, the resolvent operator has been introduced, and it was used to characterize the effect of *arbitrary* flow forcing on the integrated heat release rate. The mapping between an input field (the spatially distributed forcing) and an output scalar (the global heat release rate amplitude) involved an inner product of the forcing with the receptivity vector. In this section, a singular value decomposition of the resolvent operator is performed, in order to identify *spatially distributed* oscillation structures in the flame that maximize the response for a given input energy, as introduced in the next paragraph. This will result in a hierarchy of input fields (spatially distributed forcing structures) paired with their associated output fields (spatially distributed response structures) that is particularly useful for reduced-order modelling, and for a discussion of dominant amplification mechanisms in the flame dynamics.

6.1 Formalism

We set out with the question, which spatial distribution of forcing input $\hat{\boldsymbol{f}}$ leads to the strongest linear flow response $\hat{\boldsymbol{q}}$. Norms must be defined,

$$\|\hat{\boldsymbol{f}}\|^2 = \hat{\boldsymbol{f}}^{\mathsf{H}} \boldsymbol{M_f} \hat{\boldsymbol{f}}, \quad \|\hat{\boldsymbol{q}}\|^2 = \hat{\boldsymbol{q}}^{\mathsf{H}} \boldsymbol{M_q} \hat{\boldsymbol{q}} \tag{22}$$

where $\boldsymbol{M_f}$ and $\boldsymbol{M_q}$ are symmetric matrices that contain weight coefficients. Eq. (15) represents one special choice for such a norm definition. The matrix $\boldsymbol{M_f}$ is positive-definite, with dimensions corresponding to the forcing vector $\hat{\boldsymbol{f}}$. The dimensions of matrix $\boldsymbol{M_q}$ correspond to that of the response vector $\hat{\boldsymbol{q}}$, i.e. the total number of degrees of freedom contained in the discretized flow response. Matrix $\boldsymbol{M_q}$ may be positive semi-definite, in cases where not all flow variables or not the entire flow domain are included in the definition of $\|\hat{\boldsymbol{q}}\|^2$. In such cases, $\|\hat{\boldsymbol{q}}\|$ represents a seminorm, which is a valid choice for the resolvent formalism [38]. The gain between the squared norms of a given forcing and its associated response is found to take the form of a Rayleigh quotient,

$$\sigma^2 = \frac{\|\hat{\boldsymbol{q}}\|^2}{\|\hat{\boldsymbol{f}}\|^2} = \frac{\hat{\boldsymbol{f}}^{\mathsf{H}} \boldsymbol{P}^{\mathsf{H}} \boldsymbol{R}^{\mathsf{H}} \boldsymbol{M_q} \boldsymbol{R} \boldsymbol{P} \hat{\boldsymbol{f}}}{\hat{\boldsymbol{f}}^{\mathsf{H}} \boldsymbol{M_f} \hat{\boldsymbol{f}}}, \tag{23}$$

which can be transformed into the generalized eigenvalue problem

$$\boldsymbol{P}^{\mathsf{H}} \boldsymbol{R}^{\mathsf{H}} \boldsymbol{M_q} \boldsymbol{R} \boldsymbol{P} \hat{\boldsymbol{f}} = \sigma^2 \boldsymbol{M_f} \hat{\boldsymbol{f}}. \tag{24}$$

The operator $\boldsymbol{P}^{\mathsf{H}} \boldsymbol{R}^{\mathsf{H}} \boldsymbol{M_q} \boldsymbol{R} \boldsymbol{P}$ is Hermitian, therefore its eigenvectors $\hat{\boldsymbol{f}}_{\boldsymbol{i}}$ form an orthogonal set, in the inner-product space defined with the matrix $\boldsymbol{M_f}$, and all eigenvalues σ_i^2 are real positive. Let these eigenvalues be numbered in descending order, such that $\sigma_i^2 > \sigma_{i+1}^2$. The *optimal gain* of the forced linear system is then given by σ_1^2, and it is achieved by the optimal forcing distribution given by the leading eigenvector $\hat{\boldsymbol{f}}_{\boldsymbol{1}}$. The associated optimal flow response is named $\hat{\boldsymbol{q}}_{\boldsymbol{1}}$. The ensemble of these eigenvalues, forcing and response structures are often called the *resolvent modes* in the recent literature [57, 58, 40]. Mathematically, they represent the singular modes of a modified resolvent operator, from which the original resolvent $\boldsymbol{R}$ can be fully retrieved if all modes are known (see Eq. 11 in [40]), or reduced-order approximations can be constructed from a limited number of dominant modes [39].

Analogous to the forcing modes $\hat{\boldsymbol{f}}_{\boldsymbol{i}}$, the response modes $\hat{\boldsymbol{q}}_{\boldsymbol{i}}$ are orthogonal among one another with respect to the inner product matrix $\boldsymbol{M_q}$ [57, 58, 40], which provides a straightforward interpretation of the role of these modes for the flame dynamics. By construction, the flow is most receptive to the optimal forcing $\hat{\boldsymbol{f}}_{\boldsymbol{1}}$, which provokes a response with norm $\|\hat{\boldsymbol{q}}_{\boldsymbol{1}}\| = \sigma_1 \|\hat{\boldsymbol{f}}_{\boldsymbol{1}}\|$. Within the forcing subspace that is orthogonal to $\hat{\boldsymbol{f}}_{\boldsymbol{1}}$, the optimal way to force the flow is with the spatial structure given by $\hat{\boldsymbol{f}}_{\boldsymbol{2}}$, and so forth. If one assumes that all forcing modes are present at equal amplitude in the nonlinear terms (represented by $\hat{\boldsymbol{f}}$ in Eq. (13)), then the corresponding response modes will be found with amplitudes proportional to their gain value, dominated by the optimal mode $\hat{\boldsymbol{q}}_{\boldsymbol{1}}$.

Table 1: Gain definitions for resolvent analysis.

	norm A	norm B
forcing	$\iint_D (\lvert\hat{f}_u\rvert^2 + \lvert\hat{f}_v\rvert^2) dxdy$	$\iint_D \lvert\hat{f}_{\mathrm{CH_4}}\rvert^2 dxdy$
response	$\iint_D \lvert\hat{\omega}_T\rvert^2 dxdy$	$\iint_D \lvert\hat{\omega}_T\rvert^2 dxdy$

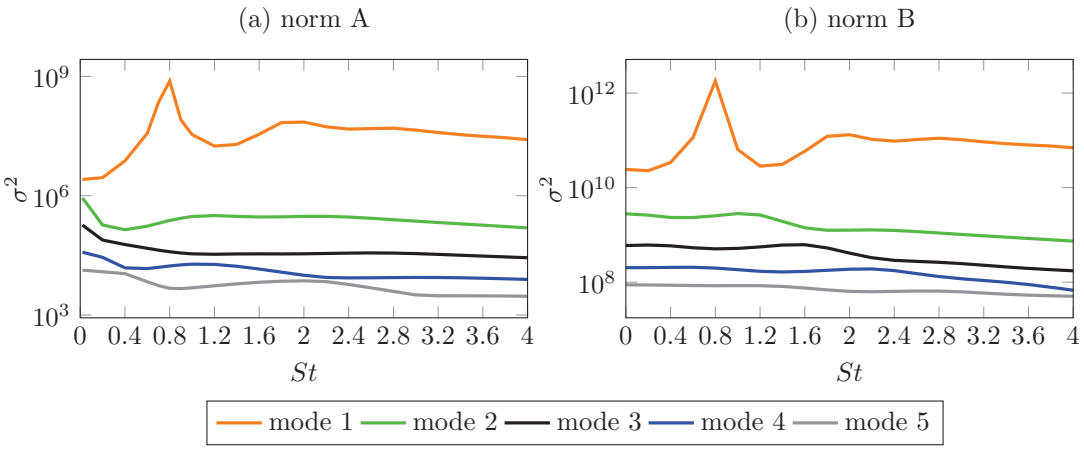

Figure 9: Gain versus Strouhal number of the five leading resolvent modes.

For the resolvent analysis, the root-mean-square (rms) amplitude of heat release rate fluctuations is chosen as the (semi-)norm of the flow response, as this provides a meaningful measure of flame unsteadiness. Moreover, it allows to identify a set of optimal and suboptimal modes. Conversely, the global heat release rate takes the form of a rank-1 norm, so it does not allow to obtain more than one mode. Two different definitions are tried for the forcing norm, given in Table 1: in the case of norm A, forcing is applied on the right-hand side of the momentum equations, with components $\hat{f}_u$ and $\hat{f}_v$; in the case of norm B, the forcing acts on the fuel concentration. In both cases, a standard L2-norm (rms amplitude) of the applied forcing is used.

The eigenvalue problem (Eq. 24) is solved using the implicitly restarted Arnoldi method from the ARPACK library. For any given frequency, the resolvent modes with the five highest gain values $(\sigma_1, \ldots, \sigma_5)$ are computed, with a relative accuracy of 10^{-12}.

6.2 Dominant dynamics in the forced flame

Gain values σ^2 of the five leading resolvent modes are plotted as functions of frequency in Fig. 9 for norms A and B. Overall, it is found that the optimal mode (mode 1) experiences a significantly higher amplification than all subsequent modes, and it can therefore be expected that the optimal response structures will dominate the flame response to arbitrary forcing input. A peak in the optimal gain curve is observed at around $St = 0.8$, suggestive of a resonance mechanism. Following the discussion in Section 5, we suspect a slightly damped ITA instability mode to exist near this frequency.

The forcing and response structures of mode 1 and mode 2 at $St = 0.8$ are presented in Fig. 10 for norm A, and in

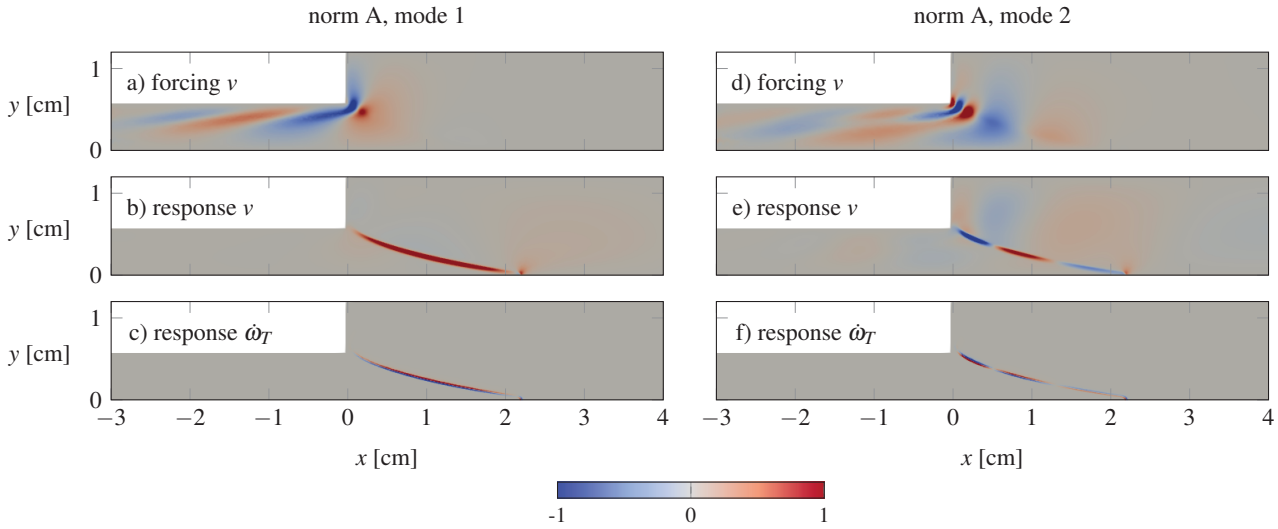

Figure 10: Forcing and response structures (real parts) of the two leading resolvent modes at $St = 0.8$, obtained with norm A. All the fields are normalised with their maximum value.

Fig. 11 for norm B. All fields are normalized here with their amplitude maximum for the sake of visualization. Turning first to the optimal resolvent mode obtained for norm A, Fig. 10b shows that the response is characterized by strong fluctuations of the transverse velocity v in the flame front. Negative values (blue) denote an inward displacement of the front, positive values (red) denote an outward displacement, consistent with the heat release rate fluctuations in Fig. 10c. Note that the real part of $\hat{\boldsymbol{q}}$ merely corresponds to a snapshot of the time-dependent perturbation $\hat{\boldsymbol{q}} \exp(i\omega t)$. When animated in time, the perturbations in the flame front are downstream-travelling waves. The red spot in Fig. 10b that emanates from the flame tip is caused by strong fluctuations of thermal expansion, related to heat release rate, in this location. An animation of mode 1 in Fig. 10 can be found in supplementary material.

The response in Figs. 10b,c is generated by a forcing input in the form of tilted downstream-travelling waves in the inflow duct, shown in Fig. 10a (transverse component). These low-level velocity perturbations are convected by the base flow towards the flame front. The optimality of the tilted forcing structures stems from the fact that perturbations near the centerline are convected faster than those near the wall; the optimal forcing is indeed organized in such a way that it generates velocity fluctuations that reach the flame front with just the right phase, so that they contribute constructively to the travelling wave perturbation of the front position.

An important feature of the flow response in Figs. 10b,c is that half a perturbation wavelength extends from the flame foot to the flame tip. This observation is again consistent with the interpretation that the gain peak at $St = 0.8$ arises from a resonance of a stable ITA mode. As evoked at the end of Section 5, the established criterion for the lowest-frequency ITA mode is an FTF phase lag of π [34, 56]. This phase lag is related to a time lag τ via the angular frequency, $\omega\tau = \pi$. For the particular case of a slot flame, according to Steinbacher *et al.* [59], the time lag τ is given by the propagation time of a downstream-travelling wave along the flame length L_f with convective phase speed c_{ph}. It follows that the wavelength λ of flame front displacement in an ITA mode is related to the flame length as

$$\frac{L_f}{c_{ph}} = \frac{\pi}{\omega} \quad \Rightarrow \quad L_f = \frac{\lambda}{2}. \tag{25}$$

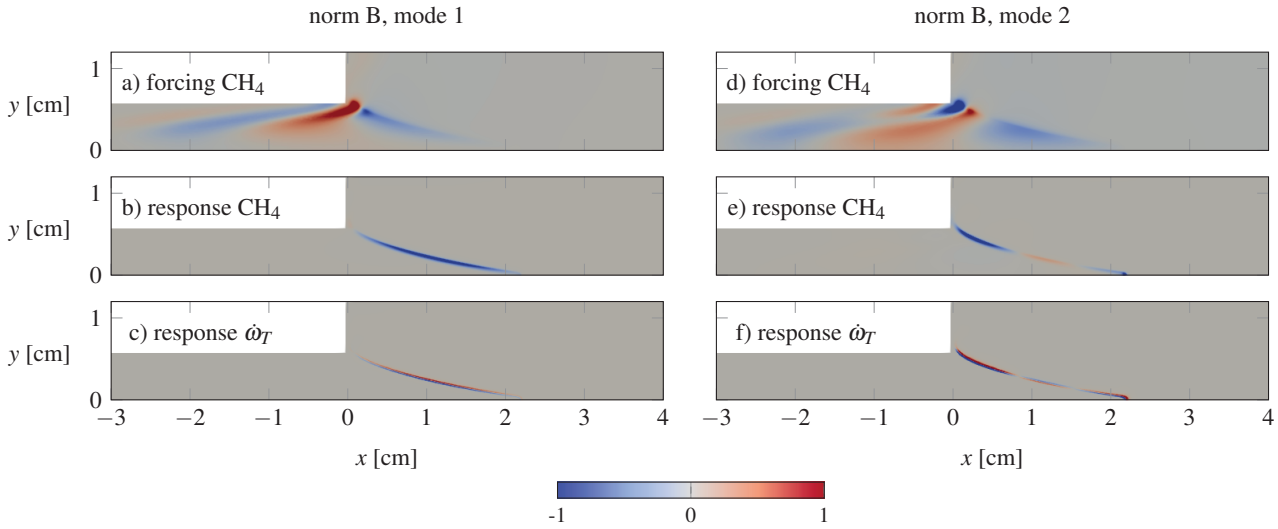

Figure 11: Forcing and response structures (real parts) of the two leading resolvent modes at $St = 0.8$, obtained with norm B. All the fields are normalised with their maximum value.

By construction, both the response and the forcing fields of mode 2 must be orthogonal to their counterparts of mode 1. In Figs. 10e,f, it is seen that the orthogonality in the response is underpinned by fitting one additional perturbation wavelength between the flame foot and the tip. As the propagation speed of perturbations along the flame front is imparted by the base flow, and therefore the same for modes 1 and 2, such a response structure can only be achieved by forcing the the upstream and downstream parts of the flame front with opposed phase. This phase opposition, between tilted forcing structures near the wall and those near the centerline in the inflow duct, can quite clearly be discerned in Fig. 10d. The forcing in this "suboptimal" mode 2 is largely destructive, and, as a consequence, much less efficient than the one of mode 1. Subsequent modes 3, 4 and 5, not shown here, extend the hierarchy of multiple wavelengths along the flame front, and corresponding finer-scale forcing structures inside the duct.

Resolvent modes obtained for the forcing of fuel fluctuations (norm B) are shown in Fig. 11, and it can immediately be seen that they contain very similar dynamics as those described for norm A. Tilted fluctuation patterns in the incoming stream are convected by the sheared base flow in such a way that they contribute constructively to one half propagating perturbation wavelength along the flame front in the case of mode 1 (Fig. 11a,b,c), whereas they act partially destructively to create one and a half wavelengths in the case of mode 2 (Fig. 11d,e,f). Comparison of fluctuations in the CH_4 concentration and in the heat release rate shows that the flame position is shifted outwards in leaner regions, and inwards in richer regions.

It is only at $St = 0.8$ that we find the particular feature of half a wavelength extending along the flame front in the optimal response, linked to the first ITA mode. More generally, the wavelength of perturbations in the flame front continuously decreases with the increase of frequency. The response fields of CH_4 (mode 1, norm B) at $St = 2.0$ and $St = 2.94$ are presented in Fig. 12. The snapshot of these responses structures are taken at the moment that a half wavelength of negative (blue) values reaches the flame tip, consistent with the snapshot at $St = 0.8$ in Fig. 11b. At these higher frequencies, the perturbation wavelengths are gradually shortened, causing more wave nodes along the front. Consistent with the above discussion of the phase lag between flame foot and flame tip, the particular Strouhal numbers in Fig. 12 give rise to 1.5 and 2.5 wavelengths along the flame front.

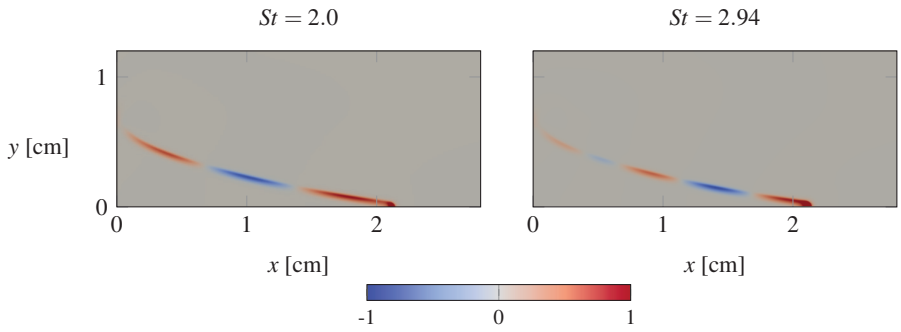

Figure 12: Response structures (real parts) of CH_4 at $St = 2.0$ and $St = 2.94$ in mode 1, obtained with norm B. All the fields are normalised with their maximum value.

In conclusion, every forcing that is applied to the linear flame model, for example in the form of nonlinearities in the actual flow, can be projected onto the basis of resolvent modes, which are orthogonal at any given frequency. Due to the strong dominance of the optimal mode gain, seen in Fig. 9, the flame response at each frequency is expected to contain the optimal response as a prevalent structure. In the present configuration, which does not include acoustic chamber resonance, the most amplified frequency of $St = 0.8$ is expected to dominate the spectrum of a stochastically driven flame.

In the present study, isothermal wall conditions are prescribed. However, flame dynamics are known to strongly depend on the wall boundary conditions [60]. Resolvent analysis may help characterise the flame response to excitations under different wall boundary conditions, which is a potential direction for future studies.

Linear resolvent analysis, as performed here in order to describe amplification mechanisms in a *laminar* flame configuration, has been shown to provide valid predictions of coherent *turbulent* dynamics in non-reacting shear flows [39, 61, 57, 58, 40, 43]. It is hoped that it will prove similarly useful for the analysis of turbulent flames.

7 Conclusions

The linear instability dynamics of a premixed slot flame have been investigated, based on the compressible flow equations with a two-step reaction model. As a validation, the linear system of equations was first shown to accurately reproduce the FTF, as obtained from nonlinear timestepping with the AVBP code, at a small fraction of the computational cost.

The linear solver was then used to characterise an input-output gain associated with the FTF, by relating the forcing energy input to the amplitude of the resulting global heat release rate fluctuations. It was demonstrated that upstream flow forcing is energetically particularly efficient at one precise frequency, suggestive of a resonance mechanism. This information could not be obtained from the FTF itself, because the FTF does not include acoustic feedback.

A specific shape of upstream velocity fluctuations is assumed in the FTF computations. Relaxing this restriction, a *receptivity* formalism was introduced, which allows to highlight the flow regions where forcing is particularly efficient in generating global heat release rate fluctuations. The receptivity field depends on the forcing frequency, and it represents itself the optimal spatial distribution of forcing input. A simple projection of any given forcing structure onto the receptivity field yields the modulus and phase of generated global heat release rate fluctuations, in the linear limit of small amplitudes. The optimal gain value, when plotted over frequency, exhibits peaks that coincide with the frequency values predicted by the π-criterion for intrinsic thermoacoustic (ITA) modes [34, 56]. It appears that the gain peaks found in the receptivity analysis are underpinned by a resonance with stable ITA modes.

Finally, a full resolvent analysis was performed, which yields for each frequency a hierarchy of orthogonal forcing

structures, and their associated orthogonal flow response structures, ranked by their input-output gain. This gain was defined in this analysis as the ratio of rms heat release rate fluctuations over rms forcing input, where the forcing was allowed to act either on the flow velocity ("norm A") or on the fuel mass fraction ("norm B"). Both types of forcing were found to be most efficient at $St = 0.8$, which is again explained as a resonance with a stable ITA mode. The optimal mode, in both norms, is significantly more efficient than all others, and it contains alone the ITA resonance peaks. A discussion of the obtained forcing/response structures highlighted the importance of constructive interaction of upstream perturbations to support a travelling-wave displacement of the flame front. Due to the shear in the base flow inside the inflow duct, the optimal forcing takes the shape of tilted waves; therefore it will be such structures in the incoming perturbations (velocity or fuel mass fraction) that elicit the strongest flame oscillations. Due to the strong separation between the optimal gain curve and all suboptimal ones, it is expected that the optimal response structures will dominate the flame response to stochastic forcing, with particularly high amplitude at the ITA resonance frequency of $St = 0.8$.

Appendix: linearized equations

The linearized governing equations and their underlying assumptions are presented here. Linearization of Eqs. (2-5) yields

$$\frac{\partial \rho'}{\partial t} = -\bar{\rho}\frac{\partial u_j'}{\partial x_j} - \bar{u}_j\frac{\partial \rho'}{\partial x_j} - \rho'\frac{\partial \bar{u}_j}{\partial x_j} - u_j'\frac{\partial \bar{\rho}}{\partial x_j}, \tag{26}$$

$$\bar{\rho}\frac{\partial u_i'}{\partial t} = -\bar{\rho}\bar{u}_j\frac{\partial u_i'}{\partial x_j} - (\bar{\rho}u_j' + \rho'\bar{u}_j)\frac{\partial \bar{u}_i}{\partial x_j} - \frac{\partial p'}{\partial x_i} + \frac{\partial \tau_{ij}'}{\partial x_j}, \tag{27}$$

$$\bar{\rho}\frac{\partial Y_k'}{\partial t} = -\bar{\rho}\bar{u}_j\frac{\partial Y_k'}{\partial x_j} - (\bar{\rho}u_j' + \rho'\bar{u}_j)\frac{\partial \bar{Y}_k}{\partial x_j} + \frac{\partial}{\partial x_j}\left(\bar{D}_k\frac{\partial Y_k'}{\partial x_j} + {D_k}'\frac{\partial \bar{Y}_k}{\partial x_j}\right) + \dot{\omega}_k'. \tag{28}$$

$$\bar{\rho}\frac{\partial}{\partial t}(h' - \frac{p'}{\bar{\rho}}) = -\bar{\rho}\bar{u}_j\frac{\partial h'}{\partial x_j} - (\bar{\rho}u_j' + \rho'\bar{u}_j)\frac{\partial \bar{h}}{\partial x_j} + \frac{\partial}{\partial x_j}\left(\bar{\alpha}\frac{\partial h'}{\partial x_j} + \alpha'\frac{\partial \bar{h}}{\partial x_j}\right) + \dot{\omega}_T'. \tag{29}$$

The linearization of ideal gas law gives $\frac{T'}{\bar{T}} = -\frac{\rho'}{\bar{\rho}} + \frac{p'}{\bar{p}}$. The fluctuation of sensible enthalpy given as $h' = \bar{c}_p T' + \sum_k Y_k'\bar{c}_{p,k}$ in [33] is simplified to $h' = \bar{c}_p T'$. The contribution of $\sum_k Y_k'\bar{c}_{p,k}$ is neglected, because $\bar{c}_{p,k}$ has similar values for all species k and $\sum_k Y_k' = 0$. The latter allows us to remove the species transport equation tracking H_2O, because Y_{H_2O}' then becomes a passive scalar, only involved in its own transport equation but not in the enthalpy equation. We have checked that involving or not the transport equation of H_2O has negligible effect on the calculation of FTF. Knowing that N_2 is another passive scalar that does not react, we finally reduce to four species transport equations tracking CH_4, O_2, CO_2 and CO.

The fluctuation of molecular viscosity writes $\mu' = b\bar{\mu}\frac{T'}{\bar{T}}$. As constant Schmidt and Prandtl numbers are assumed, the fluctuation of other transport coefficients writes ${D_k}' = \frac{\mu'}{\bar{\mu}}\bar{D}_k$ and $\alpha' = \frac{\mu'}{\mu}\bar{\alpha}$. The fluctuation of molecular stress tensor writes $\tau_{ij}' = -\frac{2\bar{\mu}}{3}\frac{\partial u_k'}{\partial x_k}\delta_{ij} + \bar{\mu}\left(\frac{\partial u_i'}{\partial x_j} + \frac{\partial u_j'}{\partial x_i}\right) - \frac{2\mu'}{3}\frac{\partial \bar{u}_k}{\partial x_k}\delta_{ij} + \mu'\left(\frac{\partial \bar{u}_i}{\partial x_j} + \frac{\partial \bar{u}_j}{\partial x_i}\right)$.

The perturbation of progress rate Q_1' writes

$$Q_1' = \bar{Q}_1\left(\left(n_{1,CH_4} + n_{1,O_2}\right)\frac{\rho'}{\bar{\rho}} + \frac{T_{a,1}T'}{\bar{T}^2} + n_{1,O_2}\frac{Y_{O_2}'}{\bar{Y}_{O_2}} + n_{1,CH_4}\frac{Y_{CH_4}'}{\bar{Y}_{CH_4}}\right). \tag{30}$$

If we denote the progress rate of second reaction as $Q_2 = Q_{f,2} - Q_{r,2}$ where $Q_{f,2} = \kappa_{f,2}[X_{\mathrm{CO}}]^{n_{2,\mathrm{CO}}}[X_{\mathrm{O_2}}]^{n_{2,\mathrm{O_2}}}$ and $Q_{r,2} = \kappa_{r,2}[X_{\mathrm{CO_2}}]^{n_{2,\mathrm{CO_2}}}$, we have $Q'_2 = Q'_{f,2} - Q'_{r,2}$, where

$$Q'_{f,2} = \bar{Q}_{f,2}\left(\left(n_{2,\mathrm{CO}} + n_{2,\mathrm{O_2}}\right)\frac{\rho'}{\bar{\rho}} + \frac{T_{a,2}T'}{\bar{T}^2} + n_{2,\mathrm{O_2}}\frac{Y'_{\mathrm{O_2}}}{\bar{Y}_{\mathrm{O_2}}} + n_{2,\mathrm{CO}}\frac{Y'_{\mathrm{CO}}}{\bar{Y}_{\mathrm{CO}}}\right), \tag{31}$$

$$Q'_{r,2} = \bar{Q}_{r,2}\left(n_{2,\mathrm{CO_2}}\frac{\rho'}{\bar{\rho}} + n_{2,\mathrm{CO_2}}\frac{Y'_{\mathrm{CO_2}}}{\bar{Y}_{\mathrm{CO_2}}}\right). \tag{32}$$

The perturbation of $\kappa_{r,2} = \frac{\kappa_{f,2}}{K}$ is not considered in this work for simplicity. The perturbation of correction functions $f_j(\phi)$ is neglected, because lean premixed flame has $f_j(\phi) \approx 1$ homogeneously in the whole domain. The perturbation of reaction rate and heat release rate write

$$\dot{\omega}'_k = W_k \sum_{j=1}^{M} \nu_{kj} Q'_j, \tag{33}$$

$$\dot{\omega}'_T = -\sum_{j=1}^{M} \Delta h^o_{f,j} Q'_j. \tag{34}$$

A similar numerical treatment as [31, 33] is applied for $\frac{Y'_{\mathrm{CH_4}}}{\bar{Y}_{\mathrm{CH_4}}}$ to avoid division by zero in $\bar{Y}_{\mathrm{CH_4}}$ which may occur from nonlinear calculation or interpolation. We choose ϵ to be 5% of the maximum value of CH_4 such that the fraction becomes $\frac{Y'_{\mathrm{CH_4}}}{\bar{Y}_{\mathrm{CH_4}}+\epsilon}$. The robustness of ϵ is verified: tuning ϵ from 5% to 15% changes around 2% in the gain of flame transfer function. A more dedicated description of linearized chemical scheme is presented in Appendix B of [33].

Acknowledgements

The authors thank the CFD group at CERFACS for providing us with their code AVBP. In this context the authors acknowledge especially the hands on help of Gabriel Staffelbach. The authors furthermore gratefully acknowledge Laurent Gicquel, Benedicte Cuenot and Franck Nicoud for fruitful discussions. Chuhan Wang is supported through a scholarship by Ecole polytechnique. The authors gratefully acknowledge the Deutsche Forschungsgemeinschaft (DFG) for funding this work within the project 441269395. The authors gratefully acknowledge the Gauss Centre for Supercomputing e.V. (www.gauss-centre.eu) for funding this project by providing computing time on the GCS Supercomputer SuperMUC-NG at Leibniz Supercomputing Centre (www.lrz.de).

Supplementary material

Supplementary video corresponding to mode 1 in Fig. 10 can be found in uploaded file fig10_mode1_video.mp4.

References

[1] P. Huerre, P. A. Monkewitz, Local and global instabilities in spatially developing flows, Annu. Rev. Fluid Mech. 22 (1) (1990) 473–537.

[2] M. Matalon, Intrinsic flame instabilities in premixed and nonpremixed combustion, Annu. Rev. Fluid Mech. 39 (2007) 163–191.

[3] T. Lieuwen, Modeling premixed combustion-acoustic wave interactions: A review, J. Propuls. Power 19 (2003) 765–781.

[4] N. Noiray, D. Durox, T. Schuller, S. Candel, A unified framework for nonlinear combustion instability analysis based on the flame describing function, J. Fluid Mech. 615 (2008) 139–167.

[5] M. P. Juniper, R. I. Sujith, Sensitivity and nonlinearity of thermoacoustic oscillations, Annu. Rev. Fluid Mech. 50 (2018) 661–689.

[6] L. Magri, Adjoint methods as design tools in thermoacoustics, Appl. Mech. Rev. 71 (2019) 020801.

[7] W. Polifke, Black-box system identification for reduced order model construction, Ann. Nucl. Energy 67 (2014) 109–128.

[8] T. Schuller, D. Durox, S. Candel, A unified model for the prediction of laminar flame transfer functions: comparisons between conical and v-flame dynamics, Combust. Flame 134 (1-2) (2003) 21–34.

[9] J. van Kampen, J. B. Kok, T. H. van der Meer, Efficient retrieval of the thermo-acoustic flame transfer function from a linearized CFD simulation of a turbulent flame, Int. J. Numer. Methods Fluids 54 (2007) 1131–1149.

[10] T. Sattelmayer, Influence of the combustor aerodynamics on combustion instabilities from equivalence ratio fluctuations, J. Eng. Gas Turbines Power 125 (2003) 11–19.

[11] J. H. Cho, T. Lieuwen, Laminar premixed flame response to equivalence ratio oscillations, Combust. Flame 140 (2005) 116–129.

[12] A. P. Dowling, Y. Mahmoudi, Combustion noise, Proc. Combust. Inst. 35 (2015) 65–100.

[13] T. Steinbacher, M. Meindl, W. Polifke, Modelling the generation of temperature inhomogeneities by a premixed flame, Int. J. Spray Combust. Dyn. 10 (2018) 111–130.

[14] D. Yang, J. Guzmán-Iñigo, A. S. Morgans, Sound generation by entropy perturbations passing through a sudden flow expansion, J. Fluid Mech. 905 (2020) R2.

[15] M. Åbom, H. Bodén, Error analysis of two-microphone measurements in ducts with flow, J. Acoust. Soc. Am. 83 (1988) 2429–2438.

[16] W. Polifke, C. O. Paschereit, K. Döbbeling, Constructive and destructive interference of acoustic and entropy waves in a premixed combustor with a choked exit, Int. J. Acoust. Vib. 6 (2001) 135–146.

[17] S. Föller, W. Polifke, Identification of aero-acoustic scattering matrices from large eddy simulation. application to a sudden area expansion of a duct, J. Sound Vib. 331 (2012) 3096–3113.

[18] B. Emerson, T. Lieuwen, M. P. Juniper, Local stability analysis and eigenvalue sensitivity of reacting bluff-body wakes, J. Fluid Mech. 788 (2016) 549–575.

[19] U. A. Qadri, G. J. Chandler, M. P. Juniper, Self-sustained hydrodynamic oscillations in lifted jet diffusion flames: origin and control, J. Fluid Mech. 775 (2015) 201–222.

[20] J. W. Nichols, P. J. Schmid, The effect of a lifted flame on the stability of round fuel jets, J. Fluid Mech. 609 (2008) 275–284.

[21] D. Moreno-Boza, W. Coenen, A. Sevilla, J. Carpio, A. Sánchez, A. Liñán, Diffusion-flame flickering as a hydrodynamic global mode, J. Fluid Mech. 798 (2016) 997–1014.

[22] U. A. Qadri, L. Magri, M. Ihme, P. J. Schmid, Using adjoint-based optimization to enhance ignition in non-premixed jets, Proc. Roy. Soc. A 477 (2021) 20200472.

[23] T. Sayadi, P. J. Schmid, Frequency response analysis of a (non-)reactive jet in crossflow, J. Fluid Mech. 922 (2021) A15.

[24] K. Oberleithner, S. Schimek, C. O. Paschereit, Shear flow instabilities in swirl-stabilized combustors and their impact on the amplitude dependent flame response: A linear stability analysis, Combust. Flame 162 (2015) 86–99.

[25] K. Oberleithner, M. Stöhr, S. H. Im, C. M. Arndt, A. M. Steinberg, Formation and flame-induced suppression of the precessing vortex core in a swirl combustor: experiments and linear stability analysis, Combust. Flame 162 (2015) 3100–3114.

[26] O. Tammisola, M. P. Juniper, Coherent structures in a swirl injector at Re= 4800 by nonlinear simulations and linear global modes, J. Fluid Mech. 792 (2016) 620–657.

[27] M. Stöhr, K. Oberleithner, M. Sieber, Z. Yin, W. Meier, Experimental study of transient mechanisms of bistable flame shape transitions in a swirl combustor, J. Eng. Gas Turb. Power 140 (1) (2018).

[28] M. Blanchard, T. Schuller, D. Sipp, P. J. Schmid, Response analysis of a laminar premixed M-flame to flow perturbations using a linearized compressible navier-stokes solver, Phys. Fluids 27 (2015) 043602.

[29] M. Blanchard, P. J. Schmid, D. Sipp, T. Schuller, Pressure wave generation from perturbed premixed flames, J. Fluid Mech. 797 (2016) 231–246.

[30] C. S. Skene, P. J. Schmid, Adjoint-based parametric sensitivity analysis for swirling M-flames, J. Fluid Mech. 859 (2019) 516–542.

[31] A. Avdonin, M. Meindl, W. Polifke, Thermoacoustic analysis of a laminar premixed flame using a linearized reactive flow solver, Proc. Combust. Inst. 37 (2019) 5307–5314.

[32] A. Albayrak, D. A. Bezgin, W. Polifke, Response of a swirl flame to inertial waves, Int. J. Spray Combust. Dyn. 10 (2018) 277–286.

[33] M. Meindl, C. F. Silva, W. Polifke, On the spurious entropy generation encountered in hybrid linear thermoacoustic models, Combust. Flame 223 (2021) 525–540.

[34] M. Hoeijmakers, V. Kornilov, I. L. Arteaga, P. de Goey, H. Nijmeijer, Intrinsic instability of flame–acoustic coupling, Combust. Flame 161 (2014) 2860–2867.

[35] E. Courtine, L. Selle, T. Poinsot, DNS of intrinsic thermoacoustic modes in laminar premixed flames, Combust. Flame 162 (2015) 4331–4341.

[36] T. Emmert, S. Bomberg, W. Polifke, Intrinsic thermoacoustic instability of premixed flames, Combust. Flame 162 (2015) 75–85.

[37] P. J. Schmid, D. S. Henningson, Stability and transition in shear flows, Springer, 2001.

[38] X. Garnaud, L. Lesshafft, P. J. Schmid, P. Huerre, Modal and transient dynamics of jet flows, Phys. Fluids 25 (2013) 044103.

[39] S. Beneddine, D. Sipp, A. Arnault, J. Dandois, L. Lesshafft, Conditions for validity of mean flow stability analysis, J. Fluid Mech. 798 (2016) 485–504.

[40] L. Lesshafft, O. Semeraro, V. Jaunet, A. V. G. Cavalieri, P. Jordan, Resolvent-based modeling of coherent wave packets in a turbulent jet, Phys. Rev. Fluids 4 (2019) 063901.

[41] A. Barbagallo, G. Dergham, D. Sipp, P. J. Schmid, J.-C. Robinet, Closed-loop control of unsteadiness over a rounded backward-facing step, J. Fluid Mech. 703 (2012) 326–362.

[42] B. J. Mckeon, A. S. Sharma, A critical-layer framework for turbulent pipe flow, J. Fluid Mech. 658 (2010) 336–382.

[43] P. Morra, O. Semeraro, D. S. Henningson, C. Cossu, On the relevance of Reynolds stresses in resolvent analyses of turbulent wall-bounded flows, J. Fluid Mech. 867 (2019) 969–984.

[44] T. L. Kaiser, L. Lesshafft, K. Oberleithner, Prediction of the flow response of a turbulent flame to acoustic pertubations based on mean flow resolvent analysis, J. Eng. Gas Turb. Power 141 (2019) 111021.

[45] M. Casel, K. Oberleithner, F. Zhang, T. Zirwes, H. Bockhorn, D. Trimis, T. L. Kaiser, Resolvent-based modelling of coherent structures in a turbulent jet flame using a passive flame approach, Combust. Flame 236 (2022) 111695.

[46] T. Schonfeld, M. Rudgyard, Steady and unsteady flow simulations using the hybrid flow solver AVBP, AIAA J. 37 (1999) 1378–1385.

[47] O. Colin, M. Rudgyard, Development of high-order Taylor–Galerkin schemes for LES, J. Comput. Phys. 162 (2000) 338–371.

[48] O. Colin, A. Benkenida, C. Angelberger, 3D modeling of mixing, ignition and combustion phenomena in highly stratified gasoline engines, Oil Gas Sci. Technol. 58 (2003) 47–62.

[49] B. Franzelli, E. Riber, L. Y. Gicquel, T. Poinsot, Large Eddy Simulation of combustion instabilities in a lean partially premixed swirled flame, Combust. Flame 159 (2012) 621–637.

[50] T. Poinsot, S. Lele, Boundary conditions for direct simulations of compressible viscous flows, J. Comput. Phys. 101 (1992) 104–129.

[51] CERFACS, CANTERA User's Guide, (https://www.cerfacs.fr/cantera/mechanisms/meth.php) (2017).

[52] M. Alnæs, A. Logg, K. Ølgaard, M. Rognes, G. Wells, Unified form language: A domain-specific language for weak formulations of partial differential equations, ACM Trans. Math. Softw. 40 (2) (2014) 1–37.

[53] W. Polifke, A. Poncet, C. Paschereit, K. Döbbeling, Reconstruction of acoustic transfer matrices by instationary computational fluid dynamics, J. Sound Vib. 245 (3) (2001) 483–510.

[54] R. Kaess, W. Polifke, T. Poinsot, N. Noiray, D. Durox, T. Schuller, S. Candel, Cfd-based mapping of the thermo-acoustic stability of a laminar premix burner, in: Proceedings of the summer program, Citeseer, 2008, p. 289.

[55] C. F. Silva, M. Merk, T. Komarek, W. Polifke, The contribution of intrinsic thermoacoustic feedback to combustion noise and resonances of a confined turbulent premixed flame, Combust. Flame 182 (2017) 269–278.

[56] M. Hoeijmakers, V. Kornilov, I. L. Arteaga, P. de Goey, H. Nijmeijer, Flame dominated thermoacoustic instabilities in a system with high acoustic losses, Combust. Flame 169 (2016) 209–215.

[57] O. Schmidt, A. Towne, G. Rigas, T. Colonius, G. Brès, Spectral analysis of jet turbulence, J. Fluid Mech. 855 (2018) 953–982.

[58] A. Towne, O. Schmidt, T. Colonius, Spectral proper orthogonal decomposition and its relationship to dynamic mode decomposition and resolvent analysis, J. Fluid Mech. 847 (2018) 821–867.

[59] T. Steinbacher, A. Albayrak, A. Ghani, W. Polifke, Consequences of flame geometry for the acoustic response of premixed flames, Combust. Flame 199 (2019) 411–428.

[60] D. Mejia, L. Selle, R. Bazile, T. Poinsot, Wall-temperature effects on flame response to acoustic oscillations, Proc. Combust. Inst. 35 (2015) 3201–3208.

[61] O. Semeraro, L. Lesshafft, V. Jaunet, P. Jordan, Modeling of coherent structures in a turbulent jet as global linear instability wavepackets: Theory and experiment, Int. J. Heat Fluid Flow 62 (2016) 24–32.